IEEE Access
Multidisciplinary | Rapid Review | Open Access Journal

Received 29 July 2022, accepted 14 August 2022, date of publication 19 August 2022, date of current version 29 August 2022.

Digital Object Identifier 10.1109/ACCESS.2022.3200303

RESEARCH ARTICLE

Characteristic Modes Analysis of a Near-Field Polarization-Conversion Metasurface for the Design of a Wideband Circularly Polarized X-Band Antenna

SIMONE GENOVESI, (Senior Member, IEEE), AND FRANCESCO ALESSIO DICANDIA
Dipartimento di Ingegneria dell'Informazione, University of Pisa, 56122 Pisa, Italy
Corresponding author: Simone Genovesi (simone.genovesi@unipi.it)

ABSTRACT A metasurface (MS) based on loop elements operating in the near field of a linearly-polarized microstrip antenna is employed to realize a circularly polarized radiated field. The properties of the loop unit cell are highlighted with the help of the Characteristic Mode Analysis that is employed for investigating the achievable linear to circular polarization conversion bandwidth and providing the guidelines for the design of the final antenna. A finite structure comprising 4×4 unit cells is tailored for achieving a circularly polarized far field within the whole X-band adopted for satellite communications (7.25 GHz-7.75 GHz, 7.9 GHz-8.4 GHz). A simple but effective single-port excitation scheme is adopted, and the overall performance are assessed by measurements on the fabricated prototype. The good agreement between simulated and measured results confirms the reliability of the proposed approach as well as the meaningful insight provided by Characteristic Modes Theory.

INDEX TERMS Characteristic modes analysis, circular polarization, metasurface, wideband, X-band, satellite communication.

I. INTRODUCTION

Circular polarization exhibits features useful in a large variety of applications. First of all, circular polarization is a fundamental asset in overcoming undesired effects of the multipath interference thanks to its intrinsic rejection of an opposite handedness polarized signal [1]. Secondly, the communication link exploiting Circularly Polarized (CP) signal is robust with respect to the relative orientation between transmitting and receiving antennas since polarization misalignment that affects linearly polarized radiators does not occur for CP ones [2]. Finally, circular polarization allows mitigating the Faraday rotation effect that the signal propagation undergoes through the ionosphere, especially degrading linearly polarized ones [3].

Several solutions have been proposed for the design of CP antennas including various kinds of microstrip patch antennas [4], [5], helix antennas [6], [7], [8], spirals [9], [10], [11] as well as dielectric resonators [12], [13]. In recent years, along with these approaches, the use of metamaterials has also been adopted to obtain a CP radiator. Some designs are based on artificial magnetic conductors that transform the electric field generated by a linearly polarized (LP) antenna into a CP wave [14], [15]. Other implementations rely on Metasurfaces (MTSs) placed on the top of a LP radiator with the aim of converting the radiated field into a CP one [16], [17], [18]. A slightly different approach is represented by a single antenna or an array that is already able to radiate a CP field whose performance in terms of bandwidth or gain are enhanced by a metasurface [19], [20], [21], [22], [23].

A novel recent approach that has been used for the design of CP antennas is represented by the Characteristic Mode Theory (CMT) [24], [25]. The CMT individuates a set of orthogonal current modes distributions, J_n, that can be stimulated on a radiator by non-resonant exciters. The current modes are intrinsically related to the size and shape of

The associate editor coordinating the review of this manuscript and approving it for publication was Bilal Khawaja.

the addressed object and are not defined by the excitation scheme [26]. In principle, these features allow to exploit a linear superposition of the current modes J_n to obtain the desired current distributions and hence the correspondent radiation pattern and electromagnetic field polarization [27], [28], [29]. Some examples of the CMT applied to the design of microstrip CP antennas can be found in [30] and [31], whereas CP radiators realized on complex platforms are illustrated in [32], [33], and [34]. CMT has also been adopted for the design of CP MTSs as described in [35], [36], and [37]. Most of these designs operates in the S and C bands but satellite applications are also very active in the X-band where adopted solutions often rely on structures such as horns or reflectarray [38], [39], [40].

This paper focuses in designing a low-profile CP antenna exploiting a MTS able to operate within whole the X-band for satellite communications, namely 7.25 GHz-7.75 GHz (space to Earth) and 7.9 GHz-8.4 GHz (Earth to space). The innovative approach consists in taking advantages of a MST superstrate based on loops elements for designing a CP antenna by resorting to the CMT. Two orthogonal characteristic modes supported by the investigated MTS have been advantageously exploited for converting the LP source into CP antenna.

This paper is organized as follows. The search for a promising candidate for the unit cell of the MTS is addressed in Section II. A first attempt to design a suitable element able to provide the necessary polarization conversion within the required frequency bandwidth is presented in the following Section III where a MTS based on a stubbed loop is analyzed. A further improvement is proposed in Section IV where a rectangular loop is tailored to fulfill the imposed constraints. Section V is devoted to the excitation of the proper current modes on the MTS whereas Section VI describes in detail the manufactured prototype and assesses the performance through measurements. Final conclusions are provided in Section VII.

II. CHARACTERISTIC MODE ANALYSIS OF THE LOOP ELEMENT

Performing a Characteristic Modes Analysis (CMA) allows to individuate a set of orthogonal currents that can be excited on a radiating platform. These currents strictly depend on the shape and size of the object with respect to the considered wavelength and are generally referred as modal currents (J_n). They are exploited as a basis for expressing any current distribution flowing on the considered object and, as a consequence of their orthogonality, the radiated field is also a weighted sum of the far field associated to each modal current [26]. Few important quantities related to CMT are essential to exploit the intrinsic design potential offered by this unique physical insight of the radiator properties and they all stem from the equation:

$$\boldsymbol{X}\boldsymbol{J}_n = \lambda_n \boldsymbol{R}\boldsymbol{J}_n \tag{1}$$

where $\boldsymbol{X}$ and $\boldsymbol{R}$ are real and symmetric matrixes representing the real and imaginary part of the impedance matrix obtained by the Method of Moments applied to the addressed object, and $\boldsymbol{J}_n$ is the modal current related to the eigenvalue of mode n (l_n). In particular, the Modal Significance (MS) of each mode n, which is calculated as:

$$MS_n = \frac{1}{|1 + j\lambda_n|} \tag{2}$$

expresses the possibility to excite that mode at a particular frequency and its value, which is independent from the applied excitation, is within [0,1]. A current mode (J_n) associated to a small eigenvalue at a certain frequency exhibits an efficient radiation and therefore a MS close to 1. Moreover, the constant phase lag between the modal current excited on the object and the tangential component of the electric field on it can be represented by the Characteristic Angle (CA):

$$\alpha_n = 180^\circ - \tan^{-1}\lambda_n \tag{3}$$

and hence a resonant mode has a CA $a_n = 180^\circ$ [41]. The total surface current on the addressed platform ($\boldsymbol{J}_{TOT}$) can be therefore expressed as a linear superposition of current modes (J_n):

$$\boldsymbol{J}_{TOT} = \sum_n a_n \boldsymbol{J}_n = \sum_n \frac{V_n^i}{1 + j\lambda_n}\boldsymbol{J}_n \tag{4}$$

where external excitation effect is considered with the term V_n^i:

$$V_n^i = \left\langle \boldsymbol{J}_n, \boldsymbol{E}^i \right\rangle = \oiint_S \boldsymbol{J}_n \cdot \boldsymbol{E}^i dS \tag{5}$$

in which the surface integral involving the external excitation $\boldsymbol{E}^i$ is evaluated on the surface S of the object. Similar considerations can be drawn for the total radiated field $\boldsymbol{E}$:

$$\boldsymbol{E} = \sum_n a_n \boldsymbol{E}_n \tag{6}$$

which is a weighted sum of the characteristic far field modes $\boldsymbol{E}_n$ [42]. The introduced quantities help to formulate the two tasks that have to be accomplished to reach the goal of designing a MTS able to generate a CP far field within frequency range of interest. The former requires that two characteristic modes, each generating a linearly polarized radiated field, must provide a 90 degrees phase difference between their characteristic CAs whereas the latter imposes that these orthogonal radiated fields exhibit the same magnitude. Most of metasurface antennas designed with CMT resort to patch-like elements [36], [37], [43], [44], [45] and very few have been devoted to preliminary investigate the properties of another basic-shaped resonator, namely the loop [46], [47], [48].

An interesting comparison between these two shapes can be done in terms of radiated far field and required footprint. A CMA is performed on both a single solid square patch and a loop that have the same side of 13 mm, being 0.5 mm the trace width of the latter. The MS of the first 10 characteristic modes

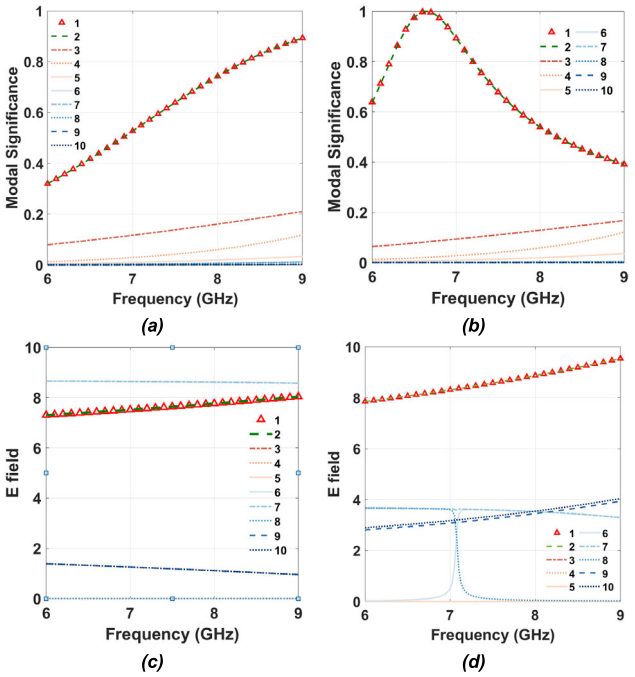

FIGURE 1. Comparison between the two considered shapes: MS of the patch (*a*), MS of the loop (*b*), electric field radiated along broadside direction for the patch (*c*) and for the loop (*d*).

is reported in Fig.1 for both of them, where the presence of two degenerate resonant modes (*i.e.,* Mode#1 and Mode#2) is expected as a result of the axial symmetry of both shapes. However, it is interesting to observe that the loop element guarantees a higher MS at a lower frequency with respect to a patch of same size. This means that the loop exhibits a lower resonance frequency for the same footprint, hence is a more compact element. A further difference in favour of the loop can be found by observing the correspondent electric radiated filed, since the dominant modal currents (*i.e.,* Mode#1 and Mode#2) provide a higher value of the radiated field along broadside. On the basis of these considerations, the loop seems a promising candidate for the design of a MTS, although the two main orthogonal modes do not satisfy the necessary 90 degrees of phase shift.

III. STUBBED LOOP FOR CP FAR FIELD

A first attempt to obtain the phase shift between the two orthogonal modes has been proposed in [46] by adding a stub of length L_s parallel to a loop side, as reported in Fig.2. The stub clearly breaks the symmetry with respect to x-axis and has proved to be useful in tailoring the phase response of co/cross polar components of the scattered field from a finite metasurface [32]. The considered structure is a finite MTS comprising 4×4 stubbed loops and the structure parameters have been optimized for fulfilling the requested conditions of the characteristic modes quantities. The choice of considering 4 unit cells for each side of the MTS has been done in order to have a radiator with small footprint. In fact, the previous section proved that the loop element is a compact one and

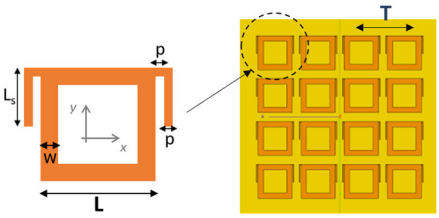

FIGURE 2. Metasurface of stubbed loops arranged in a 4 × 4 square matrix of period T = 12.5 mm. The square loop has dimensions are L = 9.5 mm, w = 1 mm, p = 0.5 mm, L_S = 4.5 mm.

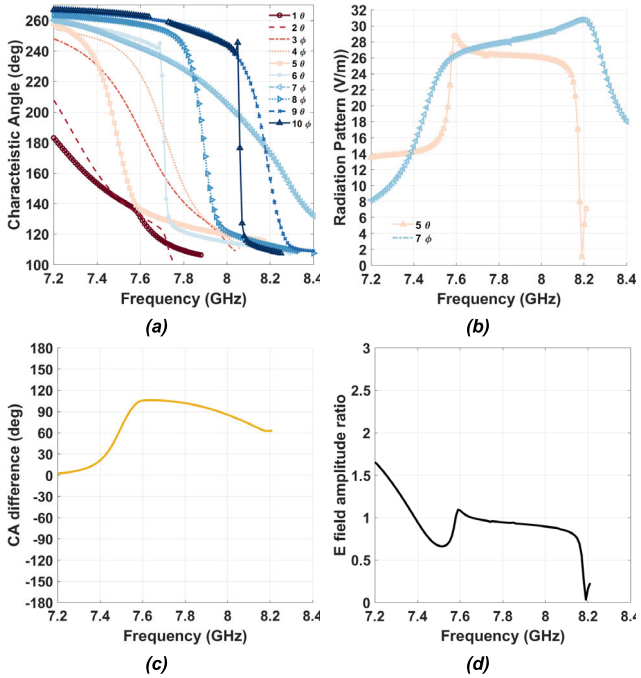

FIGURE 3. CMA for the individuation of candidate modes for the circular polarization generation: characteristic angles (*a*), radiation pattern of two suitable modes (i.e., Mode#5 and Mode#7) (*b*), characteristic angle difference between Mode#5 and Mode#7 (*c*), and ratio of the electric field amplitude along boresight for Mode#5 and Mode#7 (*d*).

therefore it is expected to have a final MTS edge with a length below $2\lambda_0$. A representative example of the performance of this kind of MTS has been obtained by considering a periodicity $T = 12.5$ mm for the loop of side $L = 9.5$ mm, width trace $w = 1$ mm, stub width $p = 0.5$ mm and length $L_S = 4.5$ mm, placed at a distance $h = 4$ mm from an infinite perfect electric conducting (PEC) ground plane.

The first ten characteristic modes have been considered and their CAs are illustrated in Fig.3 *a* where the polarization, θ or φ, of the correspondent modal far field with respect to the *xz*-plane has been also emphasized in the legend. All the simulations have been performed by using Altair FEKO. Two modes, namely Mode#5 and Mode#7, exhibit interesting properties as highlighted in Fig.3 *b-d*, where it is apparent that they have similar amplitude in the frequency range between 7.6 GHz up to around 8.1 GHz as well as a CA difference close to 90 degrees.

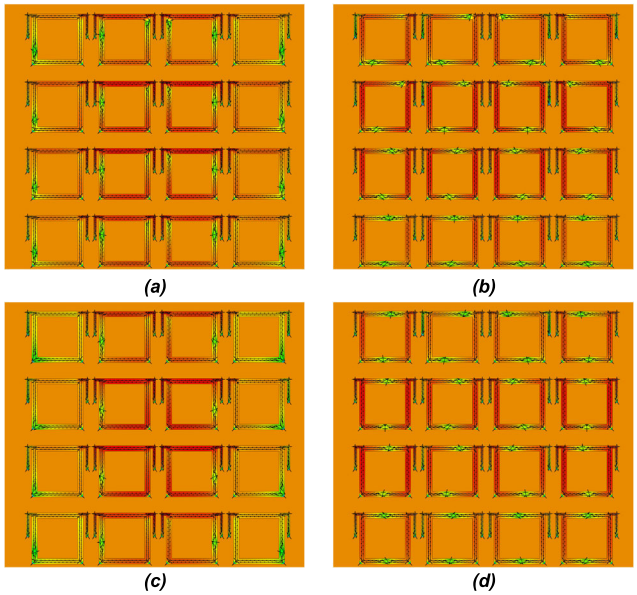

FIGURE 4. Characteristic current mode of Mode#5 at 7.8 GHz (*a*), Mode#7 at 7.8 GHz (*b*), Mode#5 at 8.1 GHz (*c*), Mode#7 at 8.1 GHz (*d*). All the current color plots are on same scale.

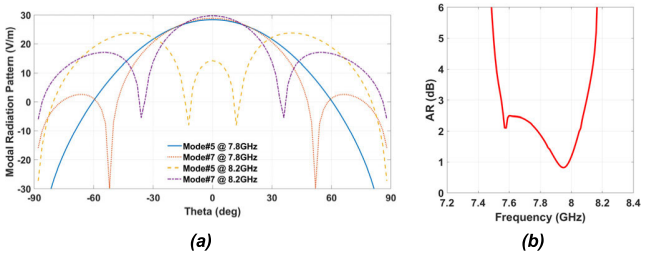

FIGURE 5. Characteristic far fields of Mode#5 and Mode#7 along xz-plane (*a*) and the overall achieved axial ratio (*b*).

The mode tracking fails in completely retrieve the radiation pattern of Mode#5 in the upper part of the frequency band of interest, however it is apparent that there is an abrupt change of the modal far field toward the boresight direction. This effect has been further investigated in Fig.4, where the characteristic current modes of Mode#5 and Mode#7 are reported at 7.8 GHz and 8.1 GHz. The former exhibits characteristic currents mainly flowing along the x-direction (Fig.4*a*) whereas in the they are along y-axis (Fig.4*b*). However, at higher frequency the currents associated with Mode#5 weaken (Fig.4*c*), especially in the two vertical sets of lateral loops. On the contrary, the level of those related to Mode#7 is not significantly altered. As a final check, the far field of these two modes have been plotted in Fig.5*a* and it is confirmed that the different modal current distribution observed Fig.4*c* determined the noticeable change of Mode#5 pattern at 8.1 GHz along broadside. This behavior has been observed in this kind of MTS configuration within the addressed frequency band, regardless of the adopted parameters. Therefore, the stub may help in providing the desired characteristic angle difference between two modes but cannot avoid the observed abrupt change in the radiated field of one of them. As a result, under the hypothesis that Mode#5 and Mode#7 are equally excited, the achievable AR with the stubbed loop is in the order of 10% (Fig.5*b*), which is not sufficient for the envisioned application.

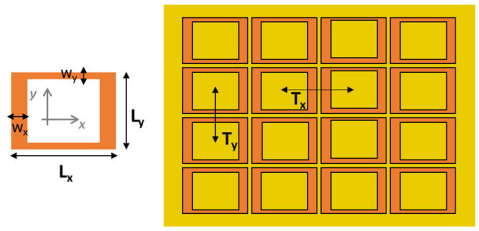

FIGURE 6. Metasurface of rectangular loops arranged in a 4 × 4 square matrix of period T_x along x-axis and T_y along y-axis. The rectangular loop has side lengths L_x and L_y along these main axes and trace widths w_x and w_y as well.

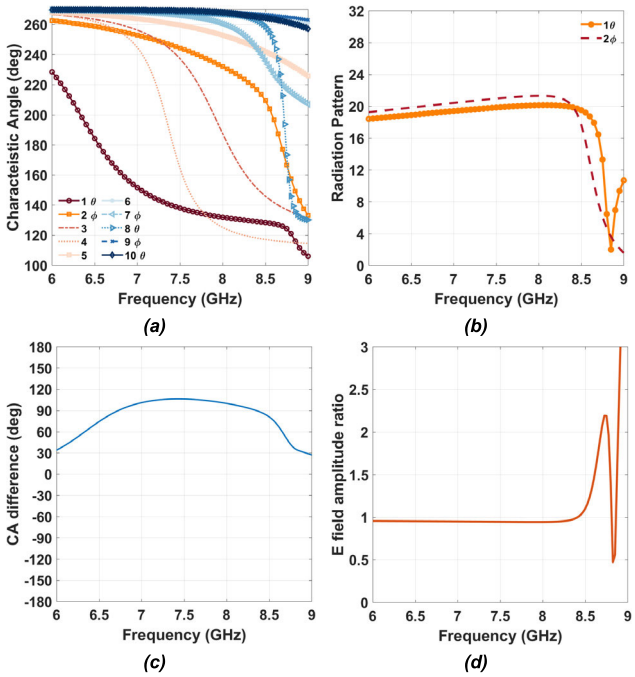

FIGURE 7. CMA for the rectangular loop element: characteristic angles (*a*), radiation pattern of two suitable modes (i.e., Mode#1 and Mode#2) (*b*), characteristic angle difference between Mode#1 and Mode#2 (*c*), and ratio of the electric field amplitude along boresight for Mode#1 and Mode#2 (*d*).

IV. RECTANGULAR LOOP FOR CP MTS DESIGN

A different asymmetry in the unit cell has to be found in order to provide a MTS able to provide the circular polarization within the addressed frequency band and therefore a rectangular loop has been considered. The loop at the basis of the finite metasurface (Fig.6) has dimension $L_x \times L_y$ and a width traces w_x and w_y. The rectangular loops are arranged into a rectangular lattice with period T_x and T_y, along the x-axis and y-axis, respectively. A thorough analysis has been carried out in order to find a couple of characteristic modes able to guarantee a characteristic angle difference close to

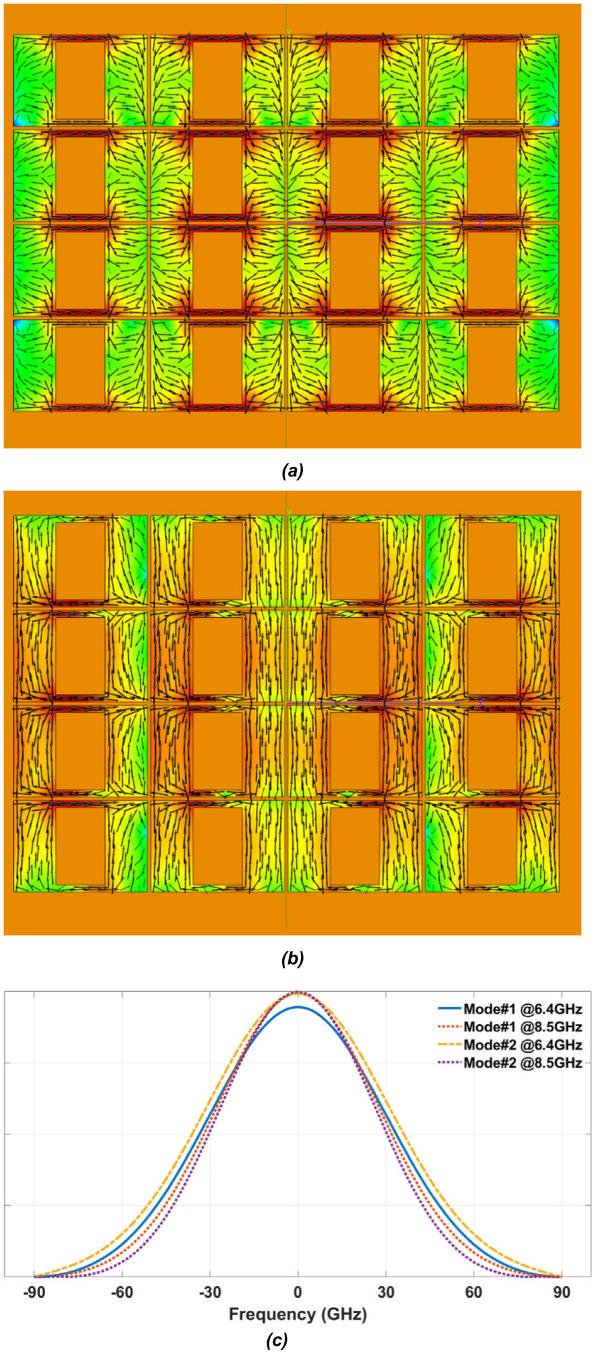

FIGURE 8. Characteristic current mode of Mode#1 at 7.5 GHz (*a*), Mode#2 at 7.5 GHz (*b*) and the related far field radiation pattern (*c*).

90 degrees in the whole frequency range and, at the same time, providing modal currents that do not determine abrupt changes in the far field pattern of the two properly-out-of-phase modes. An illustrative example that shows the remarkable potential of this kind of unit cell has been obtained by considering a periodicity $T_x = 9.75$ mm and $T_y = 6.75$ mm whereas the loop has side L_x equal to 9.5 mm and $L_y = 6.5$ mm. The considered traces width are $w_x = 3$ mm and $w_y = 3$ mm whereas the distance from the ground plane is set to $h = 3.5$mm.

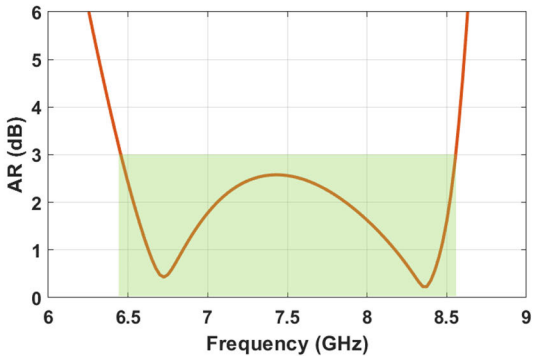

FIGURE 9. Axial ratio of the finite MTS based on the rectangular loop.

As in the previous case, the first ten characteristic modes have been considered and their CAs evaluated (Fig.7*a*) with the polarization exhibited by the related modal far field emphasized in the legend. By inspecting the radiation pattern of each mode, it has been found that some of them exhibit a constant amplitude toward the broadside direction, in particular Mode#1 and Mode#2, which radiate linearly polarized fields along θ and φ, respectively (Fig.7*b*). Moreover, these two modes exhibit a CA difference close to 90 degrees in a frequency range approximately between 6.4 GHz and 8.5 GHz (Fig.7*c*). The ratio between the amplitude of the two modes is very close to 1 in even a larger frequency interval (Fig.7*d*).

Even in this case there is an abrupt change in the radiation pattern, but this happens above the highest frequency of interest, and it is much more stable in the lower part of the spectrum under consideration.

The current modal distribution and modal radiation patterns have been analyzed to observe the difference between the rectangular loop and the stubbed one. The two modal currents exhibit strong currents along x-axis and y-axis, respectively for Mode#1 (Fig.8*a*) and Mode#2 (Fig.8*b*), at the center frequency of 7.5 GHz. The stability of the patterns has been checked also at the two extreme frequencies of the band (*i.e.,* 6.4 GHz and 8.5 GHz) and it is apparent their consistency, which further prove the pattern behavior noticed (Fig.7*d*). Supposing that Mode#1 and Mode#2 can be equally excited on the finite MTS comprising 4×4 rectangular loops, it is possible to achieve a remarkable AR bandwidth equal to 28% (Fig.9). Therefore, the CMA provides the information on the maximum achievable conversion bandwidth for this structure.

V. EXCITATION OF THE CHARACTERISTIC MODES ON THE FINITE 4 × 4 MTS

The previous results imply the equal excitation of the couple of characteristic modes exhibiting the desired features in terms of CA difference and far field amplitude along the broadside. In general, both an appropriate position and kind of the exciter allow a selective excitation of the characteristic modes over the investigated platform. To realize a

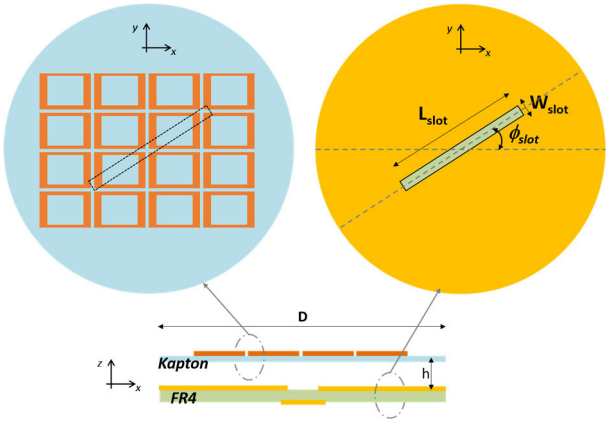

FIGURE 10. Configuration of the proposed antenna: top view of the MTS and slot (upper part) and cross section of the structure (bottom part).

fully operative prototype, it is therefore necessary to introduce an exciter able to properly stimulate Mode#1 and Mode#2. By looking at the modal current distribution shown in Fig.8*a-b* it is visible that the simplest way to efficiently stimulate Mode#1 and Mode#2 consists of applying an inductive exciter in the middle of the MTS since the selected characteristic modes are characterized by a maximum of the current distribution [43]. Therefore, the adopted configuration is represented in Fig. 10 where the MTS has been considered printed on a thin Kapton layer placed at a distance h from a slot etched on a FR4 substrate which, in turn, it is excited by the underneath microstrip line. A circular shape for the ground plane and MTS has been chosen in order to have the possibility to easily measure different angular positions of the MTS with respect to the slot. As a further step toward the fabrication the slot dimension and, most importantly, the angle φ_{slot} must be properly selected in order to provide a balanced excitation of the desired modes. The final adopted slot dimensions are $L_{slot} = 20$ mm, $W_{slot} = 3$ mm. It is worth noting that the slot has been chosen looking at the characteristic currents of Mode#1 and Mode#2 reported in Fig.8 but another source could have been chosen, such as the half loop proposed in [32]. However, this would have come at the cost of more space required and more complex feeding network.

The angle φ_{slot} plays an important role in the excitation of the desired current modes on the finite MTS and an optimal value equal to 50 degrees has been found. To understand if the excitation scheme (Fig.10) is capable to efficiently excite the desired Mode#1 and Mode#2 identified from the previous CMA, the correlation coefficient among the two desired modes and the obtained radiation pattern has been exploited to retrieve the modal power percentage [42]. More in detail, five cases have been analyzed: optimal one ($\varphi_{slot} =$ 50 degrees), plus/minus 5 degrees from the optimal φ_{slot} value and the two extreme cases with the slot parallel to the long and short side of the metasurface (Fig.11a-e). It is apparent that the modal excitation on the investigated metasurface is not constant as a function of the frequency, but it is characterized

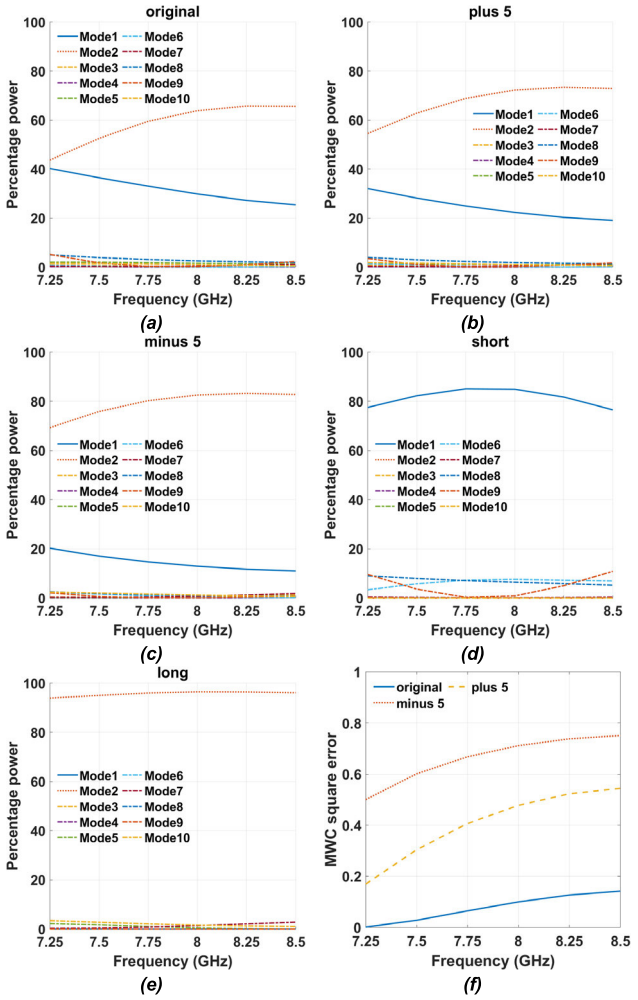

FIGURE 11. Percentage power behaviour of the two main characteristic modes as a function of frequency for different angular rotation of the slot with respect to the metasurface: (a) optimal angle, (b) optimal angle plus 5 degrees, (c) optimal angle minus 5 degrees, (d) slot parallel to the short side of the metasurface, (e) slot parallel to the long side of the metasurface and (f) Square error of the Modal Weighting Coefficient (MWC) ratio (MWC_{sq_err}).

by an opposite behaviour. In particular, the percentage power related to Mode#2 rises as a function of frequency whereas Mode#2 percentage power gently decreases with the increasing of frequency. In addition, the value of MWC_{sq_err}, the square error of the Modal Weighting Coefficient (MWC) ratio, has been evaluated as:

$$MWC_{sq\_err} = \left(\frac{MWC_1}{MWC1_2} - 1\right)^2 \tag{7}$$

to better emphasize the balance in the excitation of the modes. The ratio between the two main modes are reported for the first three cases in order to better appreciate the balance between the two modes (Fig.11f). This plot confirms that the slot angle φ_{slot} plays an essential role in the excitation of the desired current modes and the optimal value (*i.e.,* 50 degrees) guarantees the lowest modal unbalance and hence a superior axial ratio behaviour as a function of the frequency.

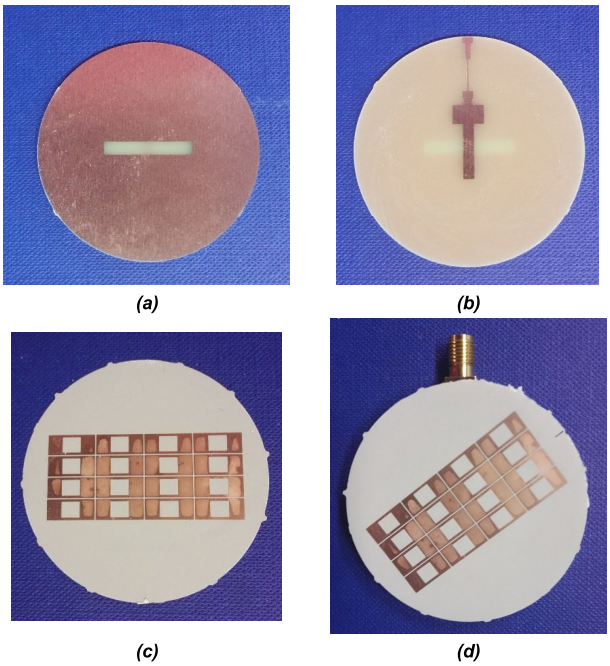

FIGURE 12. Fabricated prototype: top view of the slot exciter (*a*), underneath structure of the feeding microstrip (*b*), top view of the printed MTS (*c*), final assembled prototype (*d*).

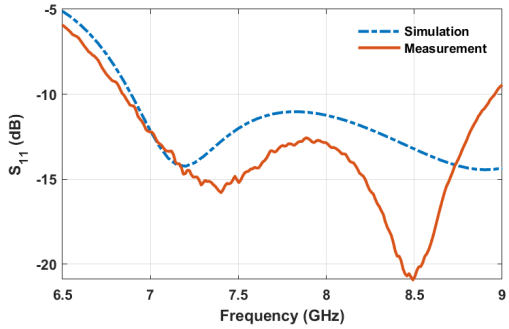

FIGURE 13. Comparison between the simulated and measured S_{11}.

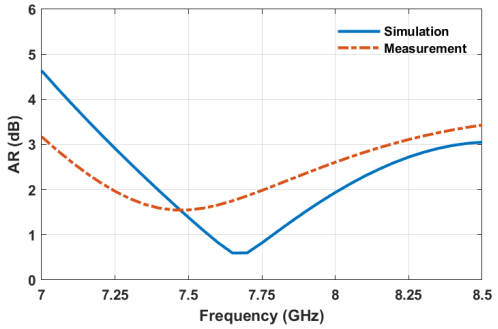

FIGURE 14. Comparison between the simulated and measured axial ratio along broadside direction.

VI. PROTOTYPE AND FINAL ASSESSMENT

A prototype of the proposed antenna has been fabricated in order to assess the performance of the proposed antenna design (Fig. 12) and it is reported in Fig. 12. The overall

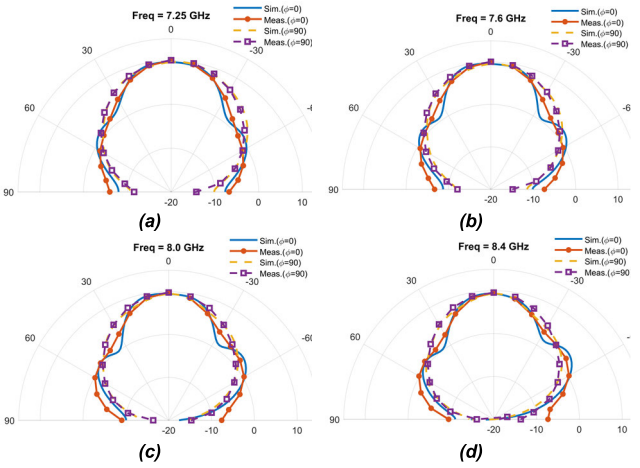

FIGURE 15. Comparison between simulated and measured normalized patterns along the principal planes ($\varphi = 0$ degrees, $\varphi = 90$ degrees) at different frequencies: 7.25 GHz (*a*), 7.6 GHz (*b*), 8.0 GHz (c) and 8.4 GHz (*d*).

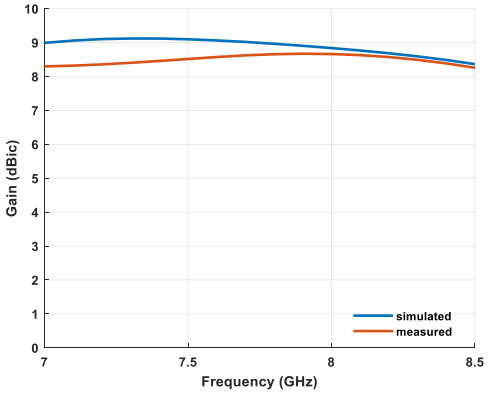

FIGURE 16. Comparison between simulated and measured gain at broadside direction.

diameter is equal to 50 mm and the distance between the MTS and the slot (h) is equal to 4 mm. As highlighted in Fig. 12*b* a microstrip lines width and length optimization has been carried out to guarantee a notable impedance matching within whole the working frequency. Two dual-polarized horn antennas (MVG QR2000, 2-18 GHz) and a four ports vector network analyzer (Anritsu Shockline MS46524B) have been employed for measurements. The comparison between the simulated and measured results are illustrated in Fig. 13 and Fig. 14. The agreement seems to be satisfactory for the S_{11} (Fig. 13) whereas a small frequency shift is observed in the axial ratio (AR) measurements along broadside direction (Fig. 14), probably due to discrepancies in the material adopted for the prototype with respect to the simulated one, in the effect of SMA soldering or in a small misalignment of the MTS.

The comparison between simulated and measured normalized radiation pattern are reported in Fig. 15 for four frequencies within the addressed bandwidth (*i.e.*, 7.25 GHz, 7.6 GHz, 8.0 GHz and 8.4 GHz) whereas the gain assessment [50] is provided in Fig. 16. They both exhibit a satisfactory

TABLE 1. Comparison with recent X-band antenna designs.

Ref.	Common bandwidth (AR < 3dB and S_{11} <-10dB)	Max Gain	Dimension
[38]	8.025–8.4 GHz (4.5%)	5 dBic	diameter: 238 mm ($6.52\lambda_0$) height: 185 mm ($6.52\lambda_0$)
[40]	8.28-8.88 GHz (7%)	14.6 dBic	62 mm × 62 mm × 22mm ($1.77\lambda_0 \times 1.77\lambda_0 \times 0.63\lambda_0$)
[51]	8.0 – 8.4 GHz (4.9%)	5.1 dBic	100 mm × 100 mm× 15mm ($2.74\lambda_0 \times 2.74\lambda_0 \times 0.41\lambda_0$)
this work	7.25 – 8.4 GHz (14.7%)	8.6 dBic	diameter: 50 mm ($1.3\lambda_0$) thickness: 5.25 mm ($0.137\lambda_0$)

level of agreement. The estimated efficiency has been found equal to 73%, being this reduction probably caused by the losses introduced by the FR4 dielectric layer employed to etch the slot and the underneath microstrip feeding line as shown in Fig.10.

Finally, a comparison with some recent designs of X-band antennas [51] is proposed in Table 1. It is possible to observe that the proposed solution has a remarkable bandwidth and a compact size.

VII. CONCLUSION

A novel metasurface exploiting a unit cell based on loop elements has been proposed for obtaining a circularly polarized radiated field starting from a linearly polarized source. The converting features of two elements based on the loop paradigm have been analyzed by using the Characteristic Mode Analysis, which has also been exploited for illustrating the design process toward the final X-band antenna for satellite communications. The tuning of the excitation source and the tailoring of the current modes excited on the metasurface has provided a compact radiator (0.137 λ_0@ 7.82 GHz) able to cover the remarkable band of interest (*i.e.,* 14.7%). Measurements on a realized prototype have assessed the performance estimated in the simulations and proved the reliability of the proposed design approach.

REFERENCES

[1] F. A. Dicandia, S. Genovesi, and A. Monorchio, "Analysis of the performance enhancement of MIMO systems employing circular polarization," *IEEE Trans. Antennas Propag.*, vol. 65, no. 9, pp. 4824–4835, Sep. 2017, doi: 10.1109/TAP.2017.2723083.

[2] W. Lin and H. Wong, "Wideband circular-polarization reconfigurable antenna with L-shaped feeding probes," *IEEE Antennas Wireless Propag. Lett.*, vol. 16, pp. 2114–2117, 2017, doi: 10.1109/LAWP.2017.2699289.

[3] E. Rignot, "Effect of Faraday rotation on L-band interferometric and polarimetric synthetic-aperture radar data," *IEEE Trans. Geosci. Remote Sens.*, vol. 38, no. 1, pp. 383–390, Jan. 2000, doi: 10.1109/36.823934.

[4] S. D. Targonski and D. M. Pozar, "Design of wideband circularly polarized aperture-coupled microstrip antennas," *IEEE Trans. Antennas Propag.*, vol. 41, no. 2, pp. 214–220, Feb. 1993, doi: 10.1109/8.214613.

[5] C. A. Balanis, *Antenna Theory: Analysis and Design*, 4th ed. Hoboken, NJ, USA: Wiley, 2016.

[6] J. D. Kraus, "The helical antenna," *Proc. IRE*, vol. 37, no. 3, pp. 263–272, Mar. 1949, doi: 10.1109/JRPROC.1949.231279.

[7] H. A. Wheeler, "A helical antenna for circular polarization," *Proc. IRE*, vol. 35, no. 12, pp. 1484–1488, Dec. 1947, doi: 10.1109/JRPROC.1947.234573.

[8] J. Tranquilla and S. Best, "A study of the quadrifilar helix antenna for global positioning system (GPS) applications," *IEEE Trans. Antennas Propag.*, vol. 38, no. 10, pp. 1545–1550, Oct. 1990, doi: 10.1109/8.59766.

[9] H. Nakano, K. Nogami, S. Arai, H. Mimaki, and J. Yamauchi, "A spiral antenna backed by a conducting plane reflector," *IEEE Trans. Antennas Propag.*, vol. AP-34, no. 6, pp. 791–796, Jun. 1986, doi: 10.1109/TAP.1986.1143893.

[10] J. Dyson, "The equiangular spiral antenna," *IRE Trans. Antennas Propag.*, vol. AP-7, no. 2, pp. 181–187, Apr. 1959, doi: 10.1109/TAP.1959.1144653.

[11] J. Kaiser, "The Archimedean two-wire spiral antenna," *IRE Trans. Antennas Propag.*, vol. 8, no. 3, pp. 312–323, May 1960, doi: 10.1109/TAP.1960.1144840.

[12] R. Chair, S. L. S. Yang, A. A. Kishk, K. F. Lee, and K. M. Luk, "Aperture fed wideband circularly polarized rectangular stair shaped dielectric resonator antenna," *IEEE Trans. Antennas Propag.*, vol. 54, no. 4, pp. 1350–1352, Apr. 2006, doi: 10.1109/TAP.2006.872665.

[13] K. W. Leung, E. H. Lim, and X. S. Fang, "Dielectric resonator antennas: From the basic to the aesthetic," *Proc. IEEE*, vol. 100, no. 7, pp. 2181–2193, Jul. 2012, doi: 10.1109/JPROC.2012.2187872.

[14] F. Yang and Y. Rahmat-Samii, "A low profile single dipole antenna radiating circularly polarized waves," *IEEE Trans. Antennas Propag.*, vol. 53, no. 9, pp. 3083–3086, Sep. 2005, doi: 10.1109/TAP.2005.854536.

[15] T. Nakamura and T. Fukusako, "Broadband design of circularly polarized microstrip patch antenna using artificial ground structure with rectangular unit cells," *IEEE Trans. Antennas Propag.*, vol. 59, no. 6, pp. 2103–2110, Jun. 2011, doi: 10.1109/TAP.2011.2143656.

[16] H. L. Zhu, S. W. Cheung, K. L. Chung, and T. I. Yuk, "Linear-to-circular polarization conversion using metasurface," *IEEE Trans. Antennas Propag.*, vol. 61, no. 9, pp. 4615–4623, Sep. 2013, doi: 10.1109/TAP.2013.2267712.

[17] G. Zhao, Y. Zhou, J. R. Wang, and M. S. Tong, "A circularly polarized dielectric resonator antenna based on quasi-self-complementary metasurface," *IEEE Trans. Antennas Propag.*, early access, Jan. 28, 2022, doi: 10.1109/TAP.2022.3145504.

[18] Q. Chen and H. Zhang, "Dual-patch polarization conversion metasurface-based wideband circular polarization slot antenna," *IEEE Access*, vol. 6, pp. 74772–74777, 2018, doi: 10.1109/ACCESS.2018.2883992.

[19] S. X. Ta and I. Park, "Compact wideband circularly polarized patch antenna array using metasurface," *IEEE Antennas Wireless Propag. Lett.*, vol. 16, pp. 1932–1936, 2017, doi: 10.1109/LAWP.2017.2689161.

[20] N. Hussain, M. Jeong, A. Abbas, T. Kim, and N. Kim, "A metasurface-based low-profile wideband circularly polarized patch antenna for 5G millimeter-wave systems," *IEEE Access*, vol. 8, pp. 22127–22135, 2020, doi: 10.1109/ACCESS.2020.2969964.

[21] N. Nasimuddin, Z. N. Chen, and X. Qing, "Bandwidth enhancement of a single-feed circularly polarized antenna using a metasurface: Metamaterial-based wideband CP rectangular microstrip antenna," *IEEE Antennas Propag. Mag.*, vol. 58, no. 2, pp. 39–46, Apr. 2016, doi: 10.1109/MAP.2016.2520257.

[22] J. A. Sheersha, N. Nasimuddin, and A. Alphones, "A high gain wideband circularly polarized antenna with asymmetric metasurface," *Int. J. RF Microw. Comput.-Aided Eng.*, vol. 29, no. 7, Jul. 2019, Art. no. e21740, doi: 10.1002/mmce.21740.

[23] K. E. Kedze, H. Wang, and I. Park, "A metasurface-based wide-bandwidth and high-gain circularly polarized patch antenna," *IEEE Trans. Antennas Propag.*, vol. 70, no. 1, pp. 732–737, Jan. 2022, doi: 10.1109/TAP.2021.3098574.

[24] B. K. Lau, M. Capek, and A. M. Hassan, "Characteristic modes: Progress, overview, and emerging topics," *IEEE Antennas Propag. Mag.*, vol. 64, no. 2, pp. 14–22, Apr. 2022, doi: 10.1109/MAP.2022.3145719.

[25] M. Capek and K. Schab, "Computational aspects of characteristic mode decomposition: An overview," *IEEE Antennas Propag. Mag.*, vol. 64, no. 2, pp. 23–31, Apr. 2022, doi: 10.1109/MAP.2021.3127527.

[26] R. F. Harrington and J. R. Mautz, "Theory of characteristic modes for conducting bodies," *IEEE Trans. Antennas Propag.*, vol. AP-19, no. 5, pp. 622–628, Sep. 1971, doi: 10.1109/TAP.1971.1139999.

[27] F. A. Dicandia, S. Genovesi, and A. Monorchio, "Null-steering antenna design using phase-shifted characteristic modes," *IEEE Trans. Antennas Propag.*, vol. 64, no. 7, pp. 2698–2706, Jul. 2016, doi: 10.1109/TAP.2016.2556700.
[28] F. A. Dicandia, S. Genovesi, and A. Monorchio, "Advantageous exploitation of characteristic modes analysis for the design of 3-D null-scanning antennas," *IEEE Trans. Antennas Propag.*, vol. 65, no. 8, pp. 3924–3934, Aug. 2017, doi: 10.1109/TAP.2017.2716402.
[29] K. K. Kishor and S. V. Hum, "A pattern reconfigurable chassis-mode MIMO antenna," *IEEE Trans. Antennas Propag.*, vol. 62, no. 6, pp. 3290–3298, Jun. 2014, doi: 10.1109/TAP.2014.2313634.
[30] Y. Chen and C. F. Wang, "Characteristic-mode-based improvement of circularly polarized U-slot and E-shaped patch antennas," *IEEE Antennas Wireless Propag. Lett.*, vol. 11, pp. 1474–1477, Nov. 2012, doi: 10.1109/LAWP.2012.2231046.
[31] H. H. Tran, N. Nguyen-Trong, and A. M. Abbosh, "Simple design procedure of a broadband circularly polarized slot monopole antenna assisted by characteristic mode analysis," *IEEE Access*, vol. 6, pp. 78386–78393, 2018, doi: 10.1109/ACCESS.2018.2885015.
[32] F. A. Dicandia and S. Genovesi, "A compact CubeSat antenna with beam-steering capability and polarization agility: Characteristic modes theory for breakthrough antenna design," *IEEE Antennas Propag. Mag.*, vol. 62, no. 4, pp. 82–93, Aug. 2020, doi: 10.1109/MAP.2020.2965015.
[33] M. R. Nikkhah, F. T. Dagefu, and N. Behdad, "Electrically small platform-based antennas for an unmanned ground vehicle," *IEEE Trans. Antennas Propag.*, vol. 68, no. 7, pp. 5189–5198, Jul. 2020, doi: 10.1109/TAP.2020.2977724.
[34] J. J. Adams, S. Genovesi, B. Yang, and E. Antonino-Daviu, "Antenna element design using characteristic mode analysis: Insights and research directions," *IEEE Antennas Propag. Mag.*, vol. 64, no. 2, pp. 32–40, Apr. 2022, doi: 10.1109/MAP.2022.3145718.
[35] M. Li, Z. Zhang, and M.-C. Tang, "A compact, low-profile, wideband, electrically controlled, tri-polarization-reconfigurable antenna with quadruple gap-coupled patches," *IEEE Trans. Antennas Propag.*, vol. 68, no. 8, pp. 6395–6400, Aug. 2020, doi: 10.1109/TAP.2020.2970073.
[36] Y. Juan, W. Yang, and W. Che, "Miniaturized low-profile circularly polarized metasurface antenna using capacitive loading," *IEEE Trans. Antennas Propag.*, vol. 67, no. 5, pp. 3527–3532, May 2019, doi: 10.1109/TAP.2019.2902735.
[37] F. A. Dicandia and S. Genovesi, "Characteristic modes analysis of non-uniform metasurface superstrate for nanosatellite antenna design," *IEEE Access*, vol. 8, pp. 176050–176061, 2020, doi: 10.1109/ACCESS.2020.3027251.
[38] E. Arnaud, J. Dugenet, K. Elis, A. Girardot, D. Guihard, C. Menudier, T. Monediere, F. Roziere, and M. Thevenot, "Compact isoflux X-band payload telemetry antenna with simultaneous dual circular polarization for LEO satellite applications," *IEEE Antennas Wireless Propag. Lett.*, vol. 19, no. 10, pp. 1679–1683, Oct. 2020, doi: 10.1109/LAWP.2020.3013989.
[39] T. Su, X. Yi, and B. Wu, "X/Ku dual-band single-layer reflectarray antenna," *IEEE Antennas Wireless Propag. Lett.*, vol. 18, no. 2, pp. 338–342, Feb. 2019, doi: 10.1109/LAWP.2018.2890766.
[40] L. Leszkowska, M. Rzymowski, K. Nyka, and L. Kulas, "High-gain compact circularly polarized X-band superstrate antenna for CubeSat applications," *IEEE Antennas Wireless Propag. Lett.*, vol. 20, no. 11, pp. 2090–2094, Nov. 2021, doi: 10.1109/LAWP.2021.3076673.
[41] E. H. Newman, "Small antenna location synthesis using characteristic modes," *IEEE Trans. Antennas Propag.*, vol. AP-27, no. 4, pp. 530–531, Jul. 1979, doi: 10.1109/TAP.1979.1142116.
[42] E. Safin and D. Manteuffel, "Reconstruction of the characteristic modes on an antenna based on the radiated far field," *IEEE Trans. Antennas Propag.*, vol. 61, no. 6, pp. 2964–2971, Jun. 2013, doi: 10.1109/TAP.2013.2251312.
[43] T. Li and Z. N. Chen, "A dual-band metasurface antenna using characteristic mode analysis," *IEEE Trans. Antennas Propag.*, vol. 66, no. 10, pp. 5620–5624, Oct. 2018, doi: 10.1109/TAP.2018.2860121.
[44] X. Gao, G. Tian, Z. Shou, and S. Li, "A low-profile broadband circularly polarized patch antenna based on characteristic mode analysis," *IEEE Antennas Wireless Propag. Lett.*, vol. 20, no. 2, pp. 214–218, Feb. 2021, doi: 10.1109/LAWP.2020.3044320.
[45] X. Yang, Y. Liu, and S.-X. Gong, "Design of a wideband omnidirectional antenna with characteristic mode analysis," *IEEE Antennas Wireless Propag. Lett.*, vol. 17, no. 6, pp. 993–997, Jun. 2018, doi: 10.1109/LAWP.2018.2828883.
[46] S. Genovesi and F. A. Dicandia, "Characteristic modes analysis for the design of a wideband circularly polarized X-band antenna," in *Proc. 16th Eur. Conf. Antennas Propag. (EuCAP)*, Mar. 2022, pp. 1–4, doi: 10.23919/EuCAP53622.2022.9768938.
[47] D. Santillan-Haro, F. Abderrazak, E. Antonino-Daviu, and M. Ferrando-Bataller, "On the bandwidth of loop antennas using characteristic mode analysis," in *Proc. IEEE Int. Symp. Antennas Propag. USNC-URSI Radio Sci. Meeting*, Jul. 2019, pp. 851–852, doi: 10.1109/APUSNCURSINRSM.2019.8889289.
[48] D. Chen, W. Yang, W. Che, and Q. Xue, "Broadband stable-gain multiresonance antenna using nonperiodic square-ring metasurface," *IEEE Antennas Wireless Propag. Lett.*, vol. 18, no. 8, pp. 1537–1541, Aug. 2019, doi: 10.1109/LAWP.2019.2919692.
[49] R. Martens, E. Safin, and D. Manteuffel, "Inductive and capacitive excitation of the characteristic modes of small terminals," in *Proc. Loughborough Antennas Propag. Conf.*, Nov. 2011, pp. 1–4, doi: 10.1109/LAPC.2011.6114141.
[50] C. J. Brochu, G. A. Morin, and J. W. Moffat, *Gain Measurement of a Cavity-Backed Spiral Antenna From 4 to 18 GHz Using the Three-Antenna Method*. Toronto, ON, Canada: Defence Research Establishment Ottawa (ONTARIO), Nov. 1998.
[51] J. Fouany, "New concept of telemetry X-band circularly polarized antenna payload for CubeSat," *IEEE Antennas Wireless Propag. Lett.*, vol. 16, pp. 2987–2991, 2017, doi: 10.1109/LAWP.2017.2756565.

SIMONE GENOVESI (Senior Member, IEEE) received the Laurea degree in telecommunication engineering and the Ph.D. degree in information engineering from the University of Pisa, Pisa, Italy, in 2003 and 2007, respectively. Since 2003, he has been collaborating with the Electromagnetic Communication Laboratory, Pennsylvania State University (Penn State), University Park. From 2004 to 2006, he was a Research Associate at the ISTI Institute of the National Research Council of Italy (ISTI-CNR), Pisa. From 2015 to 2017, he was several times a short-term Visiting Researcher at the Grenoble Institute of Technology, Valence, France, and University Rovira I Virgili, Tarragona, Spain. He is currently an Associate Professor at the Dipartimento di Ingegneria dell'Informazione, University of Pisa. He is also the Coordinator of the Additive Manufacturing Cross Laboratory founded in the framework of the Departments of Excellence ("Dipartimenti di Eccellenza") funded by the Italian Ministry of Education, University and Research. His current research interests include characteristic modes, radio frequency identification (RFID) systems, reconfigurable antennas, and metameterials.

FRANCESCO ALESSIO DICANDIA received the bachelor's and master's degrees in telecommunications engineering and the Ph.D. degree in information engineering from the University of Pisa, Pisa, Italy, in 2012, 2014, and 2018, respectively. His current research interests include reconfigurable antennas, multiple-input and multiple-output antennas, characteristic modes analysis, and chipless RFID sensors.